PLANETARY ROBOTS

Scientific exploration of challenging planetary analog environments with a team of legged robots

Philip Arm[1]†*, Gabriel Waibel[1]†, Jan Preisig[1], Turcan Tuna[1], Ruyi Zhou[1,2], Valentin Bickel[3,4], Gabriela Ligeza[5], Takahiro Miki[1], Florian Kehl[6,7,8], Hendrik Kolvenbach[1], Marco Hutter[1]

The interest in exploring planetary bodies for scientific investigation and in situ resource utilization is ever-rising. Yet, many sites of interest are inaccessible to state-of-the-art planetary exploration robots because of the robots' inability to traverse steep slopes, unstructured terrain, and loose soil. In addition, current single-robot approaches only allow a limited exploration speed and a single set of skills. Here, we present a team of legged robots with complementary skills for exploration missions in challenging planetary analog environments. We equipped the robots with an efficient locomotion controller, a mapping pipeline for online and post-mission visualization, instance segmentation to highlight scientific targets, and scientific instruments for remote and in situ investigation. Furthermore, we integrated a robotic arm on one of the robots to enable high-precision measurements. Legged robots can swiftly navigate representative terrains, such as granular slopes beyond 25°, loose soil, and unstructured terrain, highlighting their advantages compared with wheeled rover systems. We successfully verified the approach in analog deployments at the Beyond Gravity ExoMars rover test bed, in a quarry in Switzerland, and at the Space Resources Challenge in Luxembourg. Our results show that a team of legged robots with advanced locomotion, perception, and measurement skills, as well as task-level autonomy, can conduct successful, effective missions in a short time. Our approach enables the scientific exploration of planetary target sites that are currently out of human and robotic reach.

INTRODUCTION

Robotic planetary exploration is invaluable for advancing our understanding of the solar system and enabling the prospection of potential resources. The recent commitment of national and commercial entities to return to the Moon—targeting a sustainable, long-term human presence—boosted the development of robotic exploration technologies.

Many science-, exploration-, and resource extraction–relevant targets across the lunar surface lie in hard-to-reach areas or areas with substantial potential to host unknown physical surface properties. Examples include pyroclastic vents, volcanic rilles, caves, irregular mare patches, and fresh impact craters (*1*, *2*). Consequently, developing robotic exploration systems that can efficiently traverse challenging terrain without compromising their explorative, scientific, and resource prospection capabilities remains a top priority.

Several lunar exploration efforts revolve around the National Aeronautics and Space Administration's (NASA) Artemis program, which focuses on robotic and crewed science and exploration at the lunar south pole (*3*). One of the first Artemis program missions, the Volatiles Investigating Polar Exploration Rover (VIPER) (*4*), will venture into several permanently shadowed regions—cold, volatile-rich topographic depressions that have not been illuminated for millions of years (*5*–*7*). Ultimately, Artemis 3 will lead humans to the lunar south pole in 2025 (*8*). All of those missions will need to navigate the challenging south-polar terrain, including steep slopes, impact ejecta and boulder fields, and potentially anomalous physical regolith properties (*4*, *9*, *10*).

One promising way to foster the development of lunar exploration and prospection technologies is challenge-driven innovation. The European Space Agency (ESA) and the European Space Resources Innovation Centre (ESRIC) established the Space Resources Challenge (SRC) in 2021 to evaluate and advance the state of the art of robotic lunar prospecting technologies. The main technical goal of the challenge was prospecting a lunar analog environment for resource-enriched areas (REAs), meaning areas that contain minerals suitable for in situ resource utilization, such as ilmenite, rutile, and titanium dioxide. The two rounds of the challenge took place in 2021 and 2022, with the final competition in a lunar analog terrain in Luxembourg. The competition involved adverse conditions found at the lunar south pole, including previously unknown terrain, loose granular soil, high solar incidence angle illumination creating long, high-contrast shadows, and network communications with a high-latency 5.0-s round-trip time (RTT) and intermittent complete loss of signal (LoS). The SRC was an important inspiration in this work and was one of the two major field deployments of our robotic exploration team.

Here, we propose a team of legged robots for quick, efficient, and safe exploration and prospection of challenging planetary analog environments. The team approach allows us to cover a larger area, deploy a wider variety of scientific payloads, investigate more scientific targets, and gain more in-depth knowledge per target than is possible with a single-robot approach or non-teamed multirobot

[1]Robotic Systems Lab, ETH Zurich, Leonhardstrasse 21, Zurich 8092, Switzerland. [2]State Key Laboratory of Robotics and System, Harbin Institute of Technology, Harbin 150080, China. [3]Laboratory of Hydraulics, Hydrology, and Glaciology, ETH Zurich, Hönggerbergring 26, Zurich 8093, Switzerland. [4]Center for Space and Habitability, University of Bern, Gesellschaftsstrasse 6, Bern 3012, Switzerland. [5]Department of Environmental Sciences, University of Basel, Basel 4056, Switzerland. [6]Innovation Cluster Space and Aviation (UZH Space Hub), Air Force Center, University of Zurich, Dübendorf 8600, Switzerland. [7]Center for Theoretical Astrophysics and Cosmology, Institute for Computational Science, University of Zurich, Winterthurerstrasse 190, Zurich 8057, Switzerland. [8]Institute of Medical Engineering, Space Biology Group, Lucerne University of Applied Sciences and Arts, Hergiswil 6052, Switzerland.
*Corresponding author. Email: parm@ethz.ch
†These authors contributed equally to this work.

approaches. In addition, the increased redundancy allows mission completion even if multiple robots fail. To control the robotic team, the operators send high-level navigation, remote measurement, and in situ measurement tasks to the robots. The robots execute these tasks autonomously using their state-of-the-art mobility and navigation systems, as well as a complementary and redundant set of payloads. The level of autonomy allows continued scientific data collection, even if communication becomes unreliable or a complete LoS occurs. Simultaneously, the scientists in the operations team can select and prioritize scientific targets during the mission.

Until now, most planetary exploration robots relied on wheeled locomotion. Their locomotion system did not fundamentally change since the first rover, Lunokhod 1, touched down on the surface of the Moon in 1970 (*11*). Other prominent examples are the Lunar Roving Vehicle (LRV), Lunokhod 2, and Yutu 2 (*11*–*14*) and martian rovers such as Sojourner (*15*), Spirit, Opportunity (*16*), Curiosity (*17*), and Perseverance (*18*). Although these systems can build on well-tested heritage technology and provide robustness in relatively flat terrain, wheeled rovers reach their limitations on steep slopes, on loose granular terrain, and in unstructured environments. On Mars, the Spirit rover was lost in anomalously loose soil (*19*), and Opportunity got temporarily stuck in a dune (*20*). On the Moon, the Apollo 15 LRV was trapped in loose regolith and had to be manually retrieved by the astronauts (*12*). Similarly, Lunokhod 2 encountered excessive wheel sinkage (>20 cm) near Le Monnier crater (*13*). The Yutu-2 team reported that entering craters would be of great scientific interest. However, they do not target craters because of the increased probability of locomotion failure (*14*). This locomotion limitation prevents current missions from investigating high-priority targets (*1*, *2*, *21*–*23*).

Meanwhile, terrestrial legged robots have reached a high level of robustness in exploring unknown environments. Their robust locomotion system allows them to traverse unstructured, challenging natural terrains, including mud, gravel, snow, vegetation, and sand (*24*, *25*).

Several researchers have developed legged robots with the intent to use them in space in the past (*26*–*29*). Until now, we have focused on the usage of dynamically walking legged robots on steep, planetary soil analogs (*30*) and low-gravity environments (*31*–*33*), showcasing the potential of the technology. However, for these robots to be useful in real-world scenarios, they need to be advanced beyond locomotion tasks. They have to interact with their environment in realistic analog missions, for example, by deploying scientific instruments or taking samples. We advanced in this direction at the first field trial of the SRC, where we deployed a legged robot with base-mounted instruments (*34*).

Heterogeneous robotic teams have been used as a viable solution in terrestrial real-world missions. All top-ranking teams in the Defense Advanced Research Projects Agency (DARPA) Subterranean Challenge 2021 used heterogeneous robotic teams with diverse skills (*35*–*37*). To succeed in the challenge, the teams developed robust solutions for locomotion, localization, multirobot mapping, local planning, and exploration planning. In this work, we built upon these advances—specifically on the systems of our team CERBERUS (*35*)—and addressed the unique challenges presented by analog space missions, including instrument deployment, efficient and robust locomotion with robotic arms, redundancy to component or system failures, and validation in realistic missions with high-latency communication. In addition, although the robotic teams in the Subterranean Challenge were diverse in their locomotion skills, we considered diversity in scientific investigation capabilities in this work.

Several robotic teams for planetary exploration have been developed and tested in analog environments. For example, the German Aerospace Center (DLR) deployed a drone and two-wheeled robots autonomously to set up a distributed radio telescope and perform geological exploration on Mt. Etna (*38*). Although they showed a high level of autonomy, the wheeled rovers were limited in their locomotion capabilities. The German Research Center for Artificial Intelligence (DFKI) developed a heterogeneous robotic team of a wheeled and a legged robot for sample collection in a lunar analog environment (*39*). In (*40*), the authors demonstrated a teleoperated sample return mission using a robotic team in a martian analog environment. The operations team operated the robots via

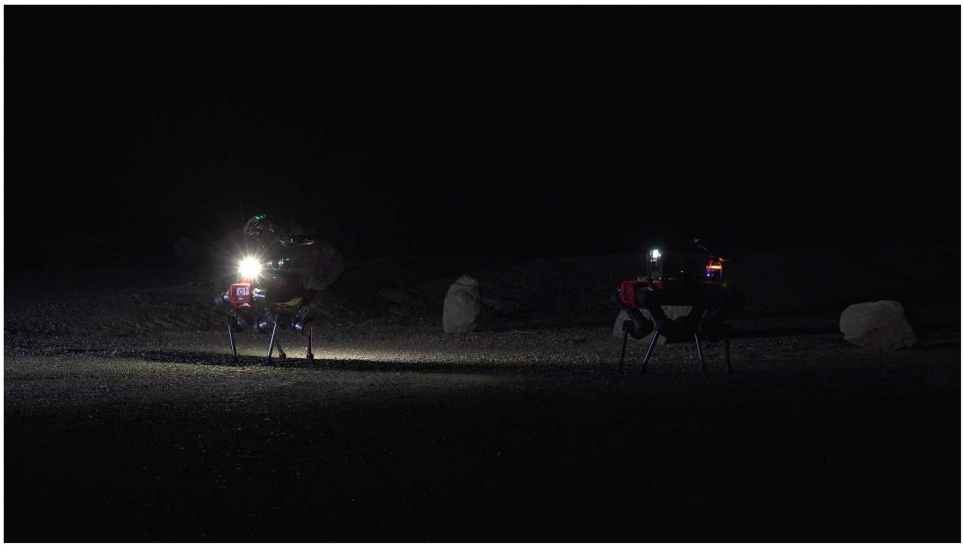

Movie 1. A team of legged robots for planetary exploration.

waypoints and tested capabilities such as sampling in isolated tests instead of the full mission deployment. More recently, NASA Jet Propulsion Laboratory (JPL) built on their NEBULA solution to explore analog martian caves with multiple Spot robots in the NASA BRAILLE project (*41*). One of the robots was equipped with a robotic arm to take close-up images and swab samples. However, the details of this work are not yet published. Last, the first heterogeneous robotic team for planetary exploration is currently operating on Mars: The Ingenuity helicopter supports the Mars 2020 mission by scouting potential targets for the Perseverance rover and inspecting targets the rover cannot access (*42*). This actual Mars mission is a remarkable example of a heterogeneous robotic team for planetary exploration.

We present our teamed exploration approach with dynamically walking robots for planetary environments (Movie 1). We designed a team of legged robots with a diverse set of scientific investigation skills and redundancy measures and validated our system in three challenging analog environments: the ExoMars locomotion test facility, a quarry site, and the competition site of the SRC. We report our results and lessons learned from these deployments and identify opportunities for future developments.

To achieve effective analog mission deployments, we developed, improved, and validated critical subsystems: We validated the baseline locomotion policy (*25*) on planetary analog terrain and developed a locomotion policy with a focus on efficiency. Our policy includes arm observations, making it robust for legged robots with robotic arms for scientific investigation in challenging environments. In addition, we built a two-pronged mapping approach for lightweight real-time online mapping and high-resolution, realistic postmission visualization. Our instance segmentation pipeline highlights potential scientific targets to support online mission planning in previously unknown environments. By distributing a balanced set of remote and close-up scientific instruments, we achieved effective and safe exploration missions. We showcase the capabilities of our legged robots in martian and lunar analog environments, demonstrating that our technology can enable robots to investigate scientifically transformative targets on the Moon and Mars that are unreachable at present using wheeled rover systems.

RESULTS

A team of legged robots for planetary exploration

The core of our system comprises a team of three four-legged robots. ANYmal (*43*) served as the base platform for all robots. Each of the three robots has a dedicated role and a unique set of payloads for exploration and scientific data collection. Figure 1A presents our team of legged robots: the Scout, the Hybrid, and the Scientist. The Scout's primary task is rapidly exploring the environment using its additional light detection and ranging (LiDAR) sensor and RGB (red, green, blue) cameras. It provides the operations team, consisting of the robot operators and planetary scientists, with an overview of the previously unknown area and allows the team to identify potential scientific targets. Its secondary task is to capture images of potential scientific targets in various spectral bands using a pan-tilt context imager augmented with a custom-built filter wheel (CTX-FW) (fig. S1). The Hybrid's main task is collecting scientific data of numerous targets using a pan-tilt context imager with an additional thermal camera (CTX-TH). Moreover, it is equipped with a base-mounted Metrohm Instant Raman Analyzer XTR DS (MIRA) with a zoom lens to acquire Raman spectra of targets of interest. The Scientist performs an in-depth scientific analysis of previously identified targets. It features a custom 6–degree of freedom (DoF) robotic arm with a MIRA on the forearm and a custom microscopic imager (MICRO) on the wrist.

Figure 1B shows a system overview. Two operators on two mission control stations sent high-level navigation, remote measurement, and in situ measurement goals to the robots. The "Scientific payload integration and deployment" section describes scientific tasks that the robot can conduct remotely using the CTX-FW and CTX-TH payloads and close-up investigations, namely, MIRA and MICRO measurements. All data packets between mission control and the robots were delayed with an RTT of 5.0 s to simulate lunar operation. Navigation goals were handled by the same module on each robot. Three-dimensional (3D) remote measurement goals were only used by the CTX imagers on the Scout and the Hybrid. The 6D in situ measurement targets were processed by the Hybrid and the Scientist. The robots sent feedback about their state, navigation images, a sparse map representation, and scientific data of targets of interest to the mission control stations.

Although all robots have their designated role, they shared many exploration capabilities and payloads, enabling a high redundancy level. If a robot failed, the operations team could reallocate tasks between the robots. Figure 2 visualizes how tasks could be reallocated for examples of exploration and measurement tasks because of the payload redundancy concept. Table S1 summarizes which scientific measurement tasks could be executed under which failure conditions.

Experimental setup on analog sites

We conducted end-to-end missions in two lunar analog environments and a locomotion validation test in a martian analog test bed. In both end-to-end analog missions, the operations team consisted of five people: A team of one robot operator and one planetary scientist each operated one of the two mission control stations. The robot operators sent tasks to the robots, and the planetary scientists selected and prioritized targets on the basis of the data received from the robots. In addition, one supervisor overlooked the mission and ensured communication between the two control teams. Both mission control stations could be used to interact with any of the robots. However, the team ensured that each robot only received commands from one control team at any given time to prevent conflicting commands, where the newer command would supersede the previous one. In the presented deployments, we used one mission control station to control the Scout and the Hybrid and the second control station to control the Scientist.

SRC, Luxembourg

One field campaign occurred at the ESA/ESRIC Space Resources Challenge in Esch-sur-Alzette, Luxembourg (September 2022). The competition area measured 1800 m^2, and the terrain was unknown before the challenge. The ground was covered in coarse, granular basalt with a substantial fine fraction (clay to silt). The light conditions closely resembled those at the lunar south pole because of a powerful illumination source at a high incidence angle in the corner of the area (Fig. 3A). The analog scenario contained several locations of interest, such as REAs, boulders, craters, and a

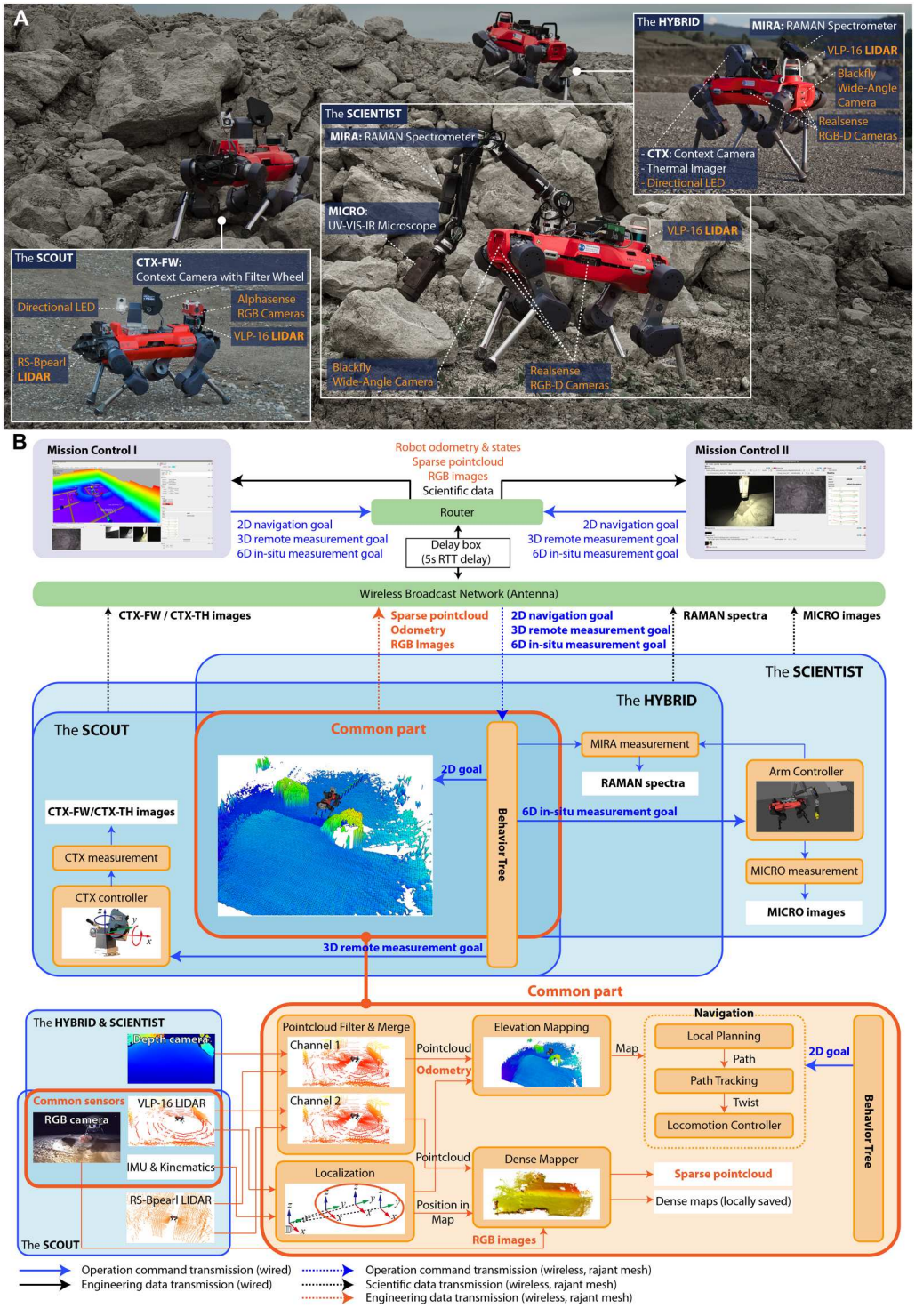

Fig. 1. System architecture of our team of legged robots. (**A**) Robotic and scientific payloads on the Scout, Scientist, and Hybrid. Robotic payloads and scientific payloads are labeled in orange and white, respectively. (**B**) High-level overview of the software architecture of our system. With a balanced combination of shared and specialized modules per robot, we designed a safe yet efficient multirobot system.

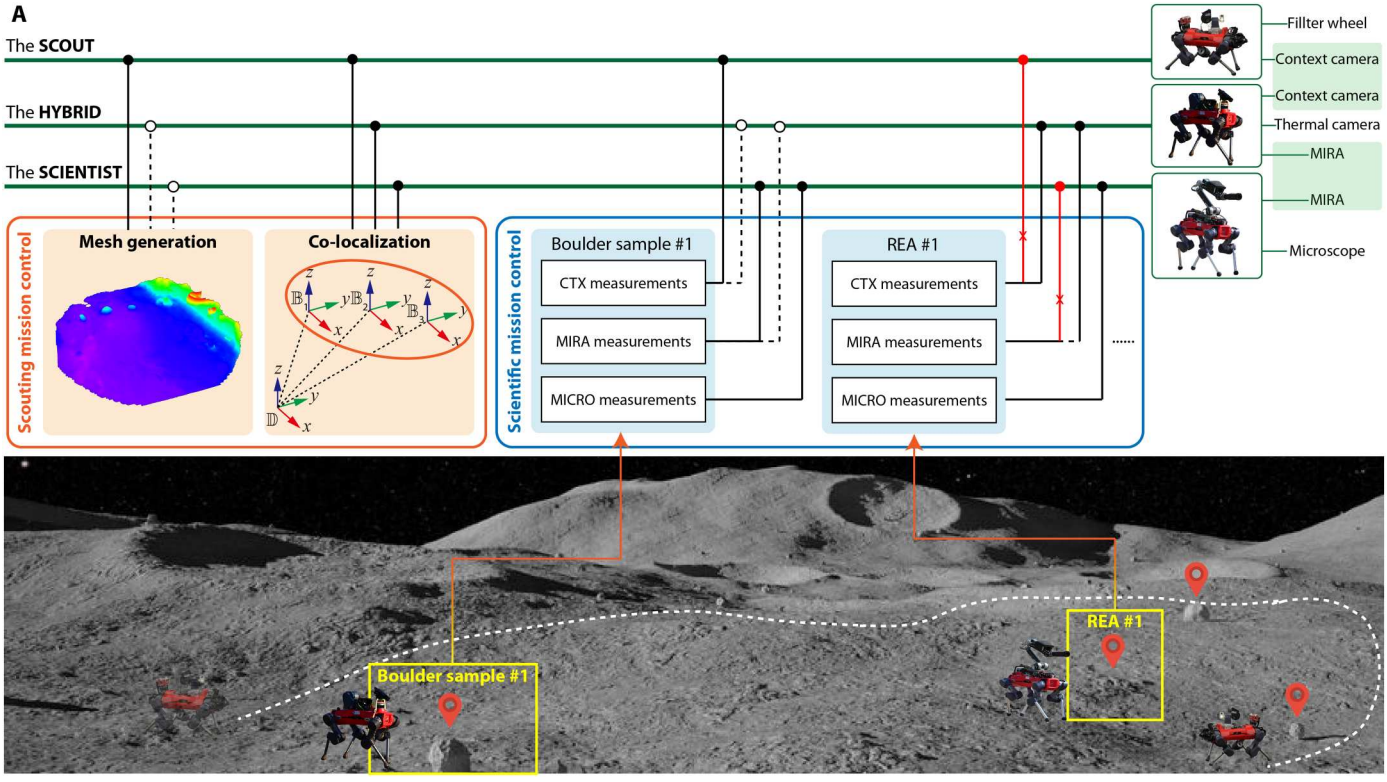

Fig. 2. Example of task allocations in our system. Task allocations are shown as solid lines. Alternative allocation paths are shown as dashed lines. When a task allocation becomes invalid, for example, because a payload or robot malfunctions (red lines), tasks can be reallocated according to our redundancy concept.

lunar habitat prototype. The mission control room was separated from the competition area with a 5.0-s RTT to communicate to all systems in the competition area. We summarize the most important objectives and rules of the SRC in table S2.

Quarry site, Switzerland

The quarry site was an active gravel quarry operated by KIBAG, situated in Neuheim, Switzerland. The quarry consists of poorly sorted fine and coarse sediments, including meter-sized boulders, leading to locomotion challenges such as sinkage and slippage, especially on steep inclines. The site includes a headwall with a maximum slope of about 20°. We simulated realistic lighting conditions in a lunar south pole scenario. To this end, we conducted the test at night to minimize the influence of naturally occurring light and illuminated the test site with a 180-W light-emitting diode (LED) lamp (Aputure LS 120D II) at a high illumination angle of roughly 87°. As shown in Fig. 4A, the illumination led to characteristic long, high-contrast shadows as expected in the vicinity of the lunar south pole. Furthermore, all communication between mission control and the robots passed through a delay simulator, which created an RTT of 5.0 s.

We selected distinct boulders on the site to simulate scientific targets of interest. Furthermore, we spread patches of basalt, ilmenite, rutile, and titanium dioxide in different mass fractions on the terrain to create realistic REAs for a lunar prospecting mission.

Locomotion validation test bed, Beyond Gravity

We used the planetary soil test bed at Beyond Gravity (fig. S2) to validate the Scout's locomotion controller (*25*) on steep, granular soil analogs. The test bed was initially designed to test the locomotion subsystem of the ExoMars rover Rosalind Franklin. It features a 6 m–by–6 m tiltable container that can be filled with various analog soil simulants. We used ESA's ES-4 martian soil simulant (*44*) and a row of Jurassic limestone plates as martian bedrock analogs for our tests. The test bed is tiltable up to 25° at a 0.1° resolution.

Analog mission results

This section provides an overview of our analog deployments: the end-to-end deployments at the SRC and in the quarry as well as the locomotion validation tests.

SRC mission overview

During the SRC, the challenge's core objectives provided by the organizers were mapping the competition area, locating boulders and REAs, and characterizing them. On that basis, we derived goals for the robotic system: These comprised mapping the entire competition area, locating REA candidates and all boulders, and providing scientific data of the boulders and potential REAs to enable trained geologists to characterize them.

Figure 3F shows the mission overview of the SRC deployment. We first deployed the Scout to map the area and used the navigation cameras and CTX-FW to help the operations team prioritize the targets of interest. After the first LoS, we decided that we had enough targets of interest to deploy the Scientist. The Scientist's

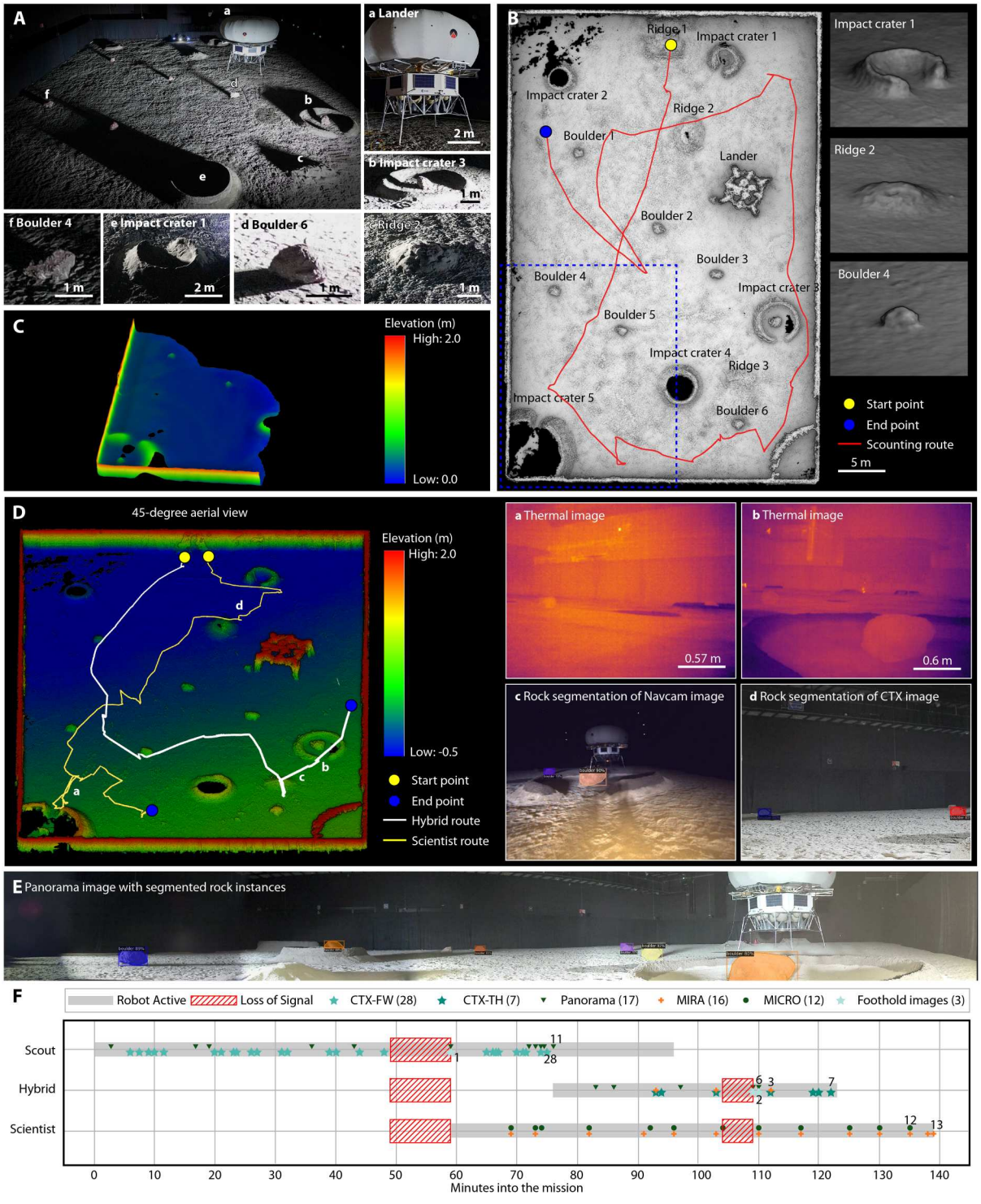

Fig. 3. Performance of our team of legged robots during the SRC. (**A**) Overview of the competition area. (**B**) Postprocessed high-resolution map of the exploration area and the associated path of the Scout. The region in the blue dotted box corresponds to (C). (**C**) Online mesh map of the Scout for target identification. (**D**) Postprocessed high-resolution height map and scientific acquisition paths of the Hybrid and the Scientist. (a and b) Thermal images acquired during the SRC. (c) Example of the rock instance segmentation of a Navcam image. (d) Example of the rock instance segmentation of a CTX image. (**E**) Example of a panorama image with rock instance segmentation acquired during the SRC. (**F**) Mission summary of the SRC.

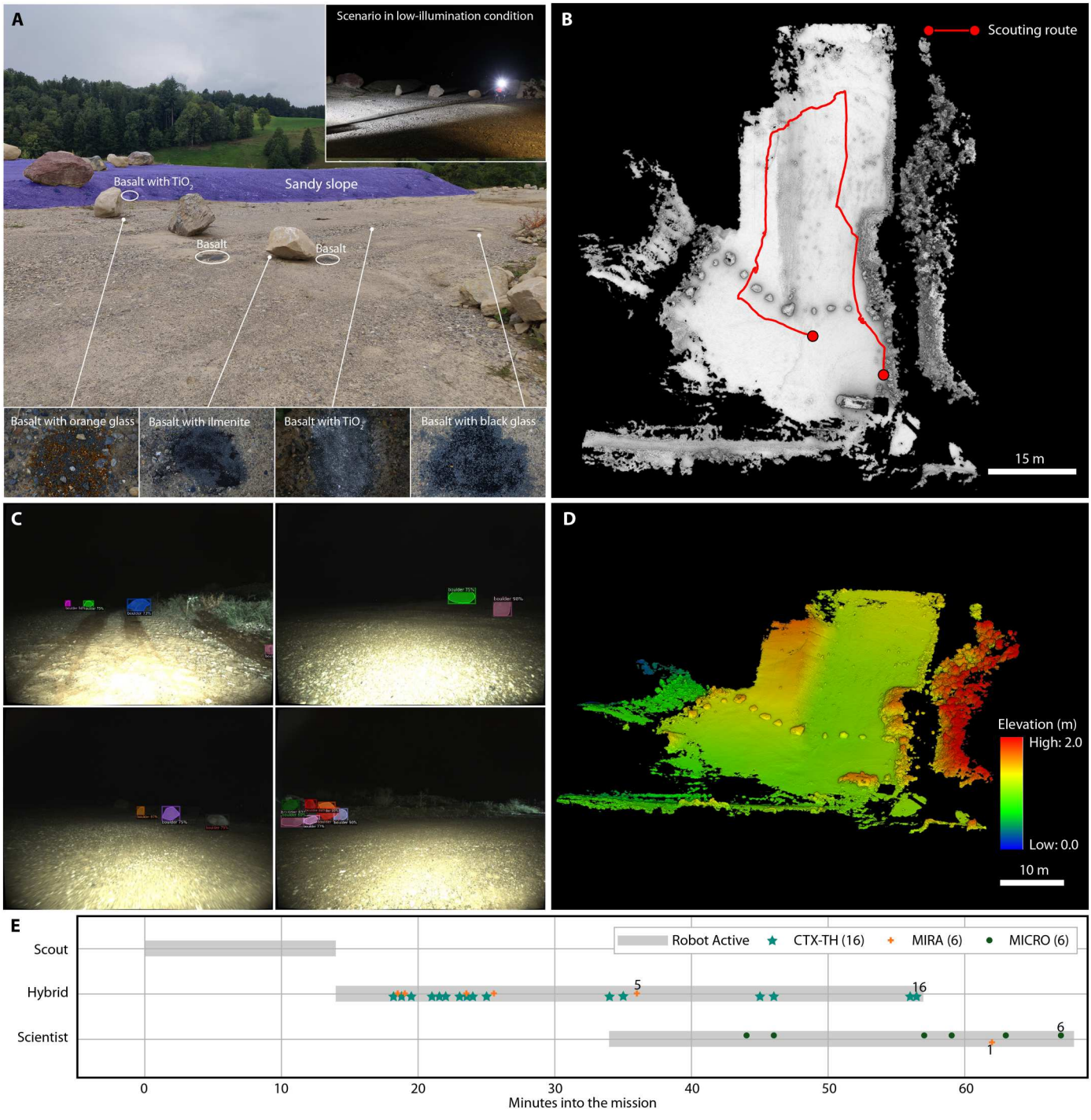

Fig. 4. Performance of our team of legged robots during the analog mission on the Neuheim quarry site. (**A**) Experimental test yard with a variety of scientific targets. (**B**) Postprocessed and shaded high-resolution map of the Neuheim quarry site with the path of the Scout. (**C**) Rock segmentation results under low-illumination conditions. (**D**) Postprocessed high-resolution elevation map of the Neuheim quarry test site. (**E**) Mission summary of the end-to-end analog deployments at the quarry. The Scout, the Hybrid, and the Scientist were all deployed sequentially with an overlap of the Hybrid and the Scientist. The whole mission duration was 68 min.

task was mainly to focus on potential REAs. After 76 min, we deployed the Hybrid to support the boulder characterization with the thermal imager and the MIRA.

We mapped 95% of the competition area, located seven of eight boulders, and identified 18 potential REAs. We prioritized five boulders for closer investigation, taking CTX-FW images of all of them and MIRA measurements of three boulders. In addition, we investigated 6 of the 18 potential REAs with MICRO and MIRA, taking several measurements per target when the data quality was insufficient.

The SRC deployment illustrates several advantages of the teamed exploration approach. Three robots operated simultaneously for 20 min because of the two mission control stations that could be used interchangeably to interact with all robots. During this time, the Scout was completing the map in yet unexplored areas, and the Hybrid and the Scientist were collecting scientific data to characterize the targets of interest. Our autonomy features and intuitive graphical user inteface (GUI) further supported deploying three robots with two operator stations. In addition, because the environment was already known after the Scout deployment, the Scientist could deploy MICRO and MIRA every 3 to 5 min, which would be unfeasible with an approach where the same robot has to map and identify targets.

Quarry mission overview

To test all payloads on a number of targets with variability, we defined a minimum of five targets to investigate with each instrument. Furthermore, we intended to map a large area to test our localization and mapping systems on a relevant scale. We accordingly defined the following mission goals for the deployment at the quarry: exploring and mapping an area of at least 1000 m^2 and identifying at least five targets of interest, such as boulders or terrain patches. To test our instruments, we set the goal to acquire measurements of at least five targets with each instrument (CTX, filter wheel, thermal imager, MIRA, and MICRO).

Figure 4E shows the mission overview of the quarry deployment. We did not use the CTX-FW on the Scout and limited the use of the MIRA on the Scientist because the hardware malfunctioned. Thus, according to our redundancy concept, we deployed the Hybrid early to take over the CTX tasks of the Scout and the MIRA tasks of the Scientist. The Scientist deployed once the operations team had identified and prioritized enough targets of interest to maximize the payload utilization on the Scientist.

In a total mission time of 68 min, we mapped an area of 1375 m^2 and identified 12 targets of interest (10 boulders and 2 area patches). We collected 16 CTX and thermal images of seven rocks, MIRA spectra of six rocks, and MICRO images of three rocks and two area patches (two MICRO datasets of the same area patch). Using our two control stations, we could efficiently control the Hybrid and the Scientist in parallel during one-third of the mission. Because of the redundancy concept in our robotic team approach, we fulfilled all mission objectives except the acquisition of filter wheel images, despite the inactive payloads. A single-robot system or a system without a redundancy concept could not have achieved the objectives related to the CTX and the MIRA measurements under these circumstances.

Fig. 5. Locomotion capability of our customized ANYmal over different challenging planetary analog terrains. (**A**) ANYmal climbs a steep sandy slope at around 20° on the Neuheim quarry site. (**B**) ANYmal escapes from the analog lunar impact crater rim during the SRC. (**C**) ANYmal escapes from deep foot sinkage in the locomotion validation test bed. (**D**) ANYmal walks over a high bedrock step.

Locomotion results

In the validation test campaign at Beyond Gravity, the Scout could climb and descend slopes of up to 25°—the maximum of the test bed—on ES-4 and bedrock using our existing locomotion control policy (*25*). On both grounds, we conducted three tests, both in ascent and descent, without a locomotion failure, which we defined as either a fall or a failure to continue the traverse, for example, due to slippage. Even on the maximum slope of the test bed, the robot reached a top speed of 0.7 m/s, outperforming state-of-the-art systems that can climb such inclinations (table S3). We conducted additional tests at a 10° slope on ES-4 with steps of bedrock and very loose hills in all directions. The robot could negotiate the hills despite the high sinkage (Fig. 5C) and seamlessly transitioned high steps between ES-4 and bedrock (Fig. 5D).

Our developed controller for the Hybrid and Scientist enabled similar robustness as the existing baseline controller (*25*) but with added heavy payloads such as the robotic arm. The moving robotic arm did not impede the Scientist while walking on flat terrain (fig. S3 and movie S1). In addition, with a static arm, the robot consumed 15% less power in a mock mission on flat ground when using our controller compared with the baseline controller (see Supplementary Results).

During the mission deployments in the quarry and the SRC, the robots traversed steep granular slopes up to 20° (Fig. 5A) and a crater rim (Fig. 5B). At the SRC, the robots covered a total distance of 358 m of granular terrain (Fig. 3, B and D). The Scientist, carrying the robotic arm, showed the same level of robustness as the Scout and the Hybrid. During all pretests and mission deployments, no single locomotion failure occurred on any of the robots.

Mapping and target identification

We used a lightweight mesh representation for online operations and a dense mapping framework for mission postprocessing in both analog missions (Fig. 6). Furthermore, we ran an instance segmentation pipeline on our navigation cameras and CTX images to identify and highlight boulders as potential targets of interest for the operations team, substantially reducing the operational overhead. Figures 3 (C to E) and 4 (C to E) show the mapping and perception results in the quarry and at the SRC, respectively.

The robot sent a downsampled point cloud in a 9-m radius around the robot to mission control. The mission control PC generated the mesh and fused single mesh instances automatically to gradually build a mesh map of the covered area. Offloading the meshing operation to the mission control PC allowed us to transmit a small point cloud instead of a heavy map. Figure 3C shows a fraction of the mesh map of the SRC built with three mesh instances. Boulders 4 and 5 and impact craters 4 and 5 are distinguishable in the mesh. Together with the navigation cameras, the resolution of the mesh map allowed the operations team to identify and mark these targets of interest for further investigation. Therefore, the resolution was high enough to understand the robot's environment, select targets on the mesh map, and make mission scheduling decisions while still allowing the map to be transferred over the network.

Figures 3D (c and d) and 4C show the instance segmentation output on the navigation cameras in the SRC and quarry missions, respectively. The images show that, even under difficult lighting conditions, the pipeline could identify and highlight boulders in the image, supporting the operations team in the target identification. In addition, we segmented selected panoramic images (Fig. 3E).

Aside from the online mesh to guide operations, all robots maintained a high-resolution point cloud map in both missions for postmission visualization. Figure 3B shows the postprocessed and shaded dense map of the complete SRC competition environment, with the path of the Scout overlaid. We explored 95% of the area with the Scout within 96 min, where most of the environment and the scientific targets were already identified after 50 min. Similarly, Fig. 4B shows the dense map created during the quarry mission. In addition, we colored the dense maps by elevation (Figs. 3D and 4D) to create a topographic overview of the environment. For example, the headwall in the quarry is visible in the top left part of the map. Furthermore, we created colored maps (figs. S4 and S5) by projecting the navigation camera colors onto the point cloud.

Scientific data of targets of interest

Once the operations team identified and prioritized targets of interest, they could send remote measurement and in situ measurement tasks to all robots (Fig. 7). Figure 8 shows an example of the scientific data that we could gather during the SRC. We acquired images in five visual spectral ranges at two zoom levels using CTX-FW (Fig. 8A). The low-zoom image shows the target's size, shape, and geomorphic context. The high-zoom image provides information about the target's surface texture, including the presence of millimeter- to centimeter-scale vesicles, the rock's lithology, and the distribution of minerals. Both low-zoom and high-zoom images indicate that all boulders in the SRC were porous basalts with aphanitic (fine-grained) textures. The high-zoom images with the filter wheel enabled us to study the relative reflectance of each target and compute five-point spectra. We color-corrected selected RGB images with images from a robot-mounted color calibration card.

Figure 8B shows in situ measurement results of a potential REA during the SRC. We collected microscopic images in six different spectral bands [white, red, green, blue, ultraviolet (UV), and infrared (IR)], allowing us to compute the target's five-point spectrum. The images show the coarse granular basalt regolith, which covered the whole competition area at the SRC. MICRO images enabled us to investigate the grain size distribution and presence of potential resources. The MIRA Raman spectrum of the basaltic regolith in Fig. 8B shows, for example, a prominent peak at 952 cm^{-1}.

DISCUSSION

Using a team of legged robots with powerful locomotion capabilities, a mapping pipeline for online and offline visualization, and segmentation tools for target identification allowed us to collect a substantial amount of scientific data in planetary analog missions with limited mission time. Compared with the single-robot approach that we deployed at the first SRC field trial (*34*), we could drastically increase the quality and quantity of scientific data products. The specialization of our robots allowed a high payload utilization, as demonstrated at the SRC, where the Scientist robot deployed the MIRA and MICRO instruments every 3 to 5 min. In a multirobot approach without specialization, for example, without a dedicated scout robot, every robot would invest a substantial part of the mission time in mapping and target identification, limiting the high-return instruments' payload utilization.

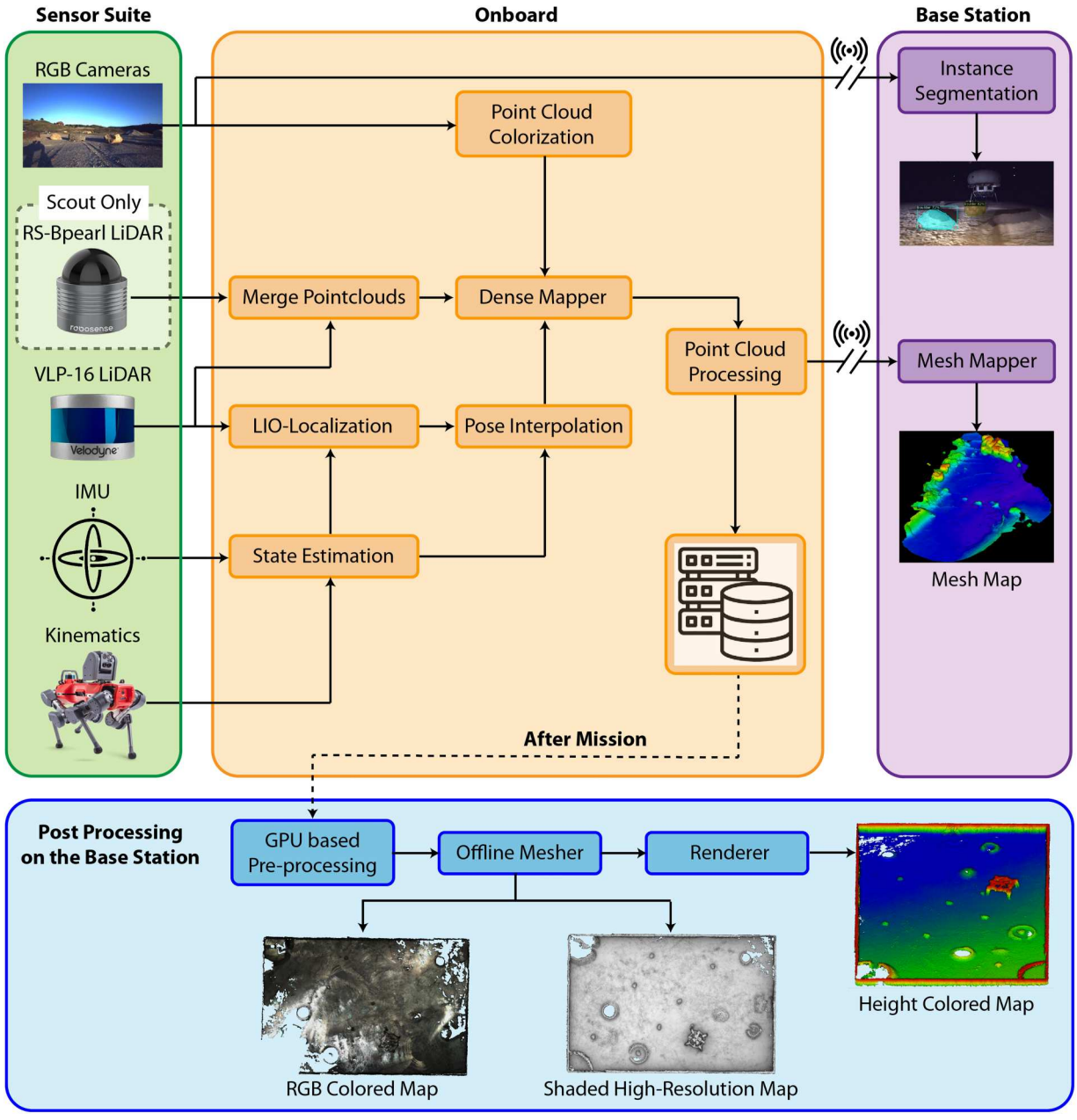

Fig. 6. Mission support mapping and localization modules. The blue area represents the postmission operations, whereas the other modules are active during the mission.

The quarry deployment showed the importance of the redundancy concept. We could still fulfill six of seven mission goals despite two malfunctioning payloads. Although we did not experience a robot failure in the deployments, our redundancy concept would allow us to still accomplish most mission goals.

Our payload selection features a balanced mix of remote and in situ science, but it was subject to budget and time constraints. Other instruments, for example, x-ray fluorescence spectrometers (XRF), as used by other teams at the SRC, performed better at identifying REAs. Further expanding our scientific instrument suite, for example, with an XRF or laser-induced breakdown spectrometer (LIBS), would increase the quality and diversity of the mission's science outputs. In addition, adapting our system to allow sample return to a lander with more capable scientific instruments would be a valuable expansion to increase the mission's scientific output.

One lesson from our field deployments is that an RTT of 5 s in the communication between mission control and the robot notably affected operations. Standard, reliable protocols such as the Transmission Control Protocol (TCP) are not suitable in this setting. When using the User Datagram Protocol (UDP), we had to reduce the data size of products, such as point clouds and images, to decrease the probability of a single packet loss occurring within the transfer of a data product. Furthermore, every operator interaction cost valuable mission time. We tackled this issue by providing

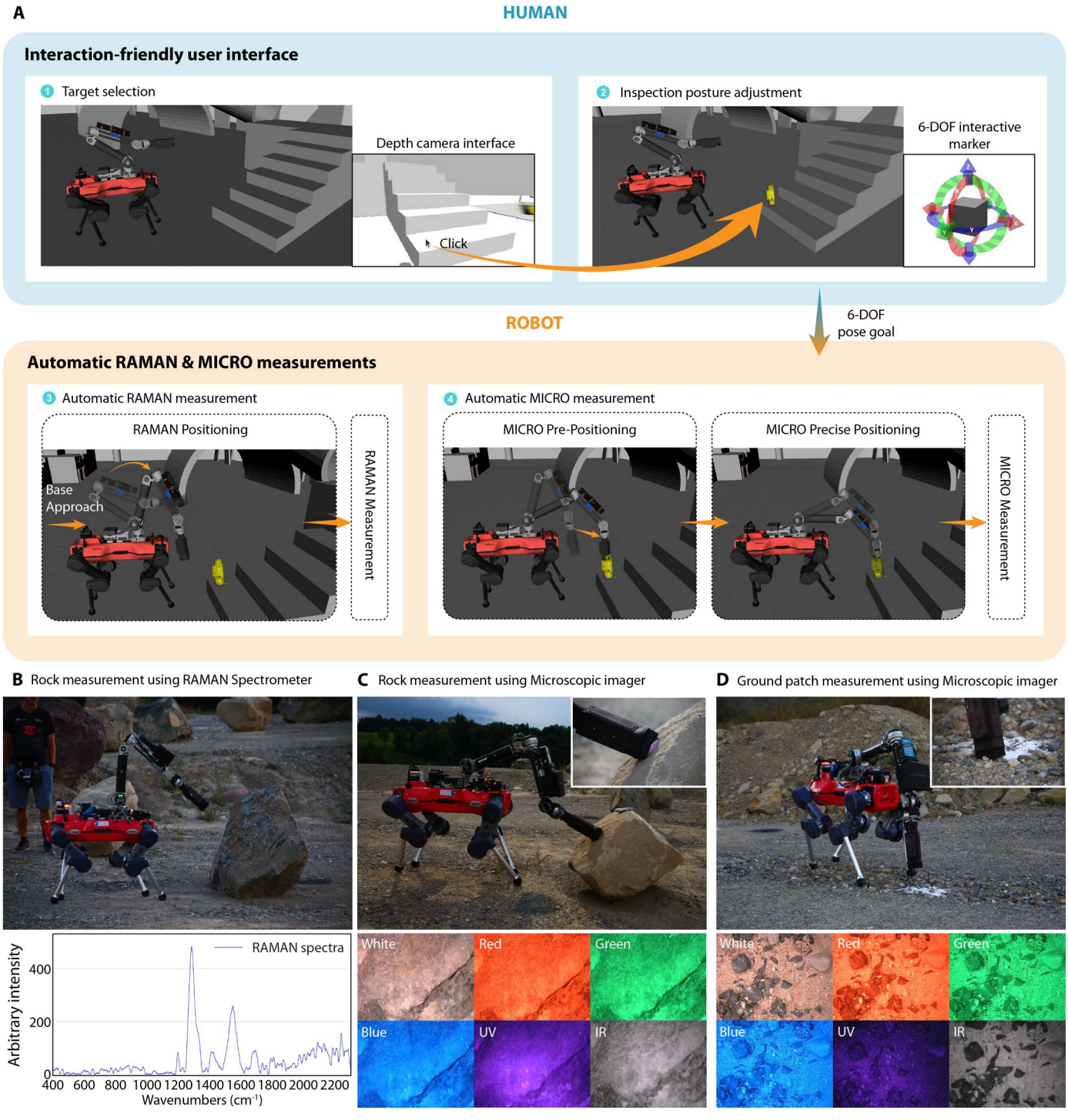

Fig. 7. In situ measurement task workflow. (**A**) The operator selects the desired target in the depth camera interface to define the instrument pose. The pose can be adjusted using a 6-DoF interactive marker. The robot receives the 6-DoF goal and uses it to deploy the scientific instruments at the desired location. (**B**) Boulder measurement using the MIRA Raman spectrometer and associated data products. (**C**) Boulder measurement using MICRO and associated data products. (**D**) Ground patch measurement using MICRO and associated data products.

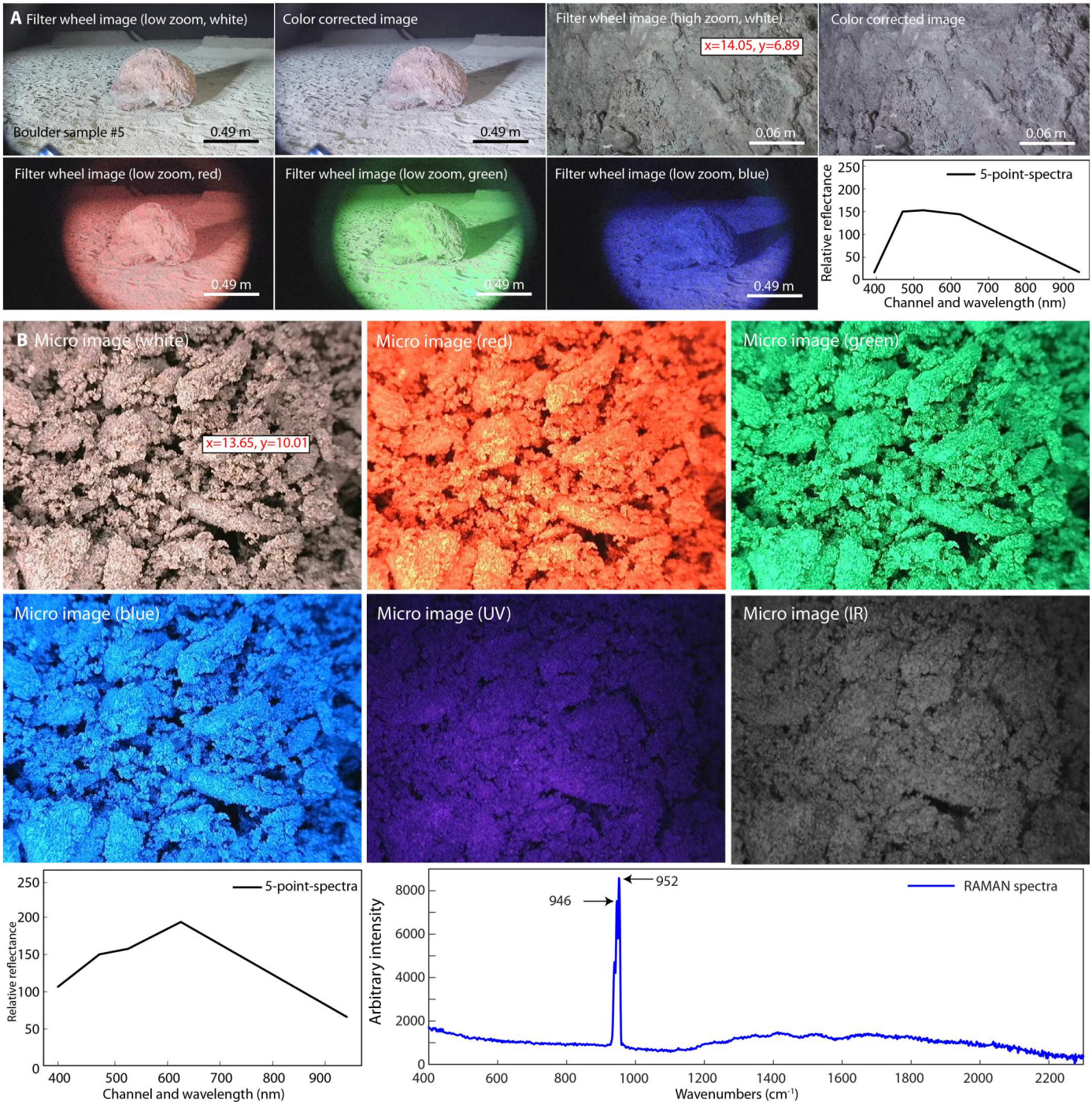

Fig. 8. Examples of scientific data products at the SRC. (**A**) Multispectral visual data acquired by the CTX-FW of boulder #5. The images show a vesicular basaltic boulder. (**B**) MICRO and Raman data products of a REA candidate. The images and spectra show the basaltic soil of the competition area. The relative reflectance has an arbitrary scale.

lightweight, expressive data to the operators, such as the mesh map, and using task-level autonomy. Hence, every task execution only required one operator interaction. However, a more in-depth analysis of suitable protocols and compression technologies could further alleviate this problem.

A key finding in our deployments was the importance of the human aspect: The robots could execute single tasks autonomously, but the human operators still had to prioritize and allocate tasks. This decision-making can be time-consuming and difficult, especially because the operators must balance the time required for the decision-making process with the mission time. An algorithmic

approach to decision-making and task allocation could improve the mission return. The algorithm could either aid the operations team or, ideally, be implemented in an autonomy module on the robots to allow longer-term or even full-mission autonomy. However, besides semantic scene understanding, this requires automatic interpretation of scientific data products such as images and spectra, which is an open challenge. Furthermore, more robot-to-robot communication is needed to build collaborative maps, allocate tasks without mission control in the loop, and allow for more involved interaction and collaboration between multiple robots.

A higher level of autonomy will additionally improve the system's scalability to applications with even more challenging communication, such as Mars exploration. Moreover, it will allow scaling of the approach to a higher number of robots without increasing the workload on the operations team. Required modules to increase the level of autonomy are a safe, multi-goal planner to visit identified targets, automatic target identification and prioritization as stated above, and automatic task allocation to the robots based on the robot-specific skillset.

In this work, we used legged robots with different scientific investigation skills but almost identical locomotion skills. In future deployments, a more heterogeneous approach could be advantageous. Drones would enable fast terrain mapping; wheeled robots, with limited mobility but higher battery life, could investigate easy-to-reach targets; whereas the legged robots focused on hard-to-access areas.

Last, a relevant research stream is the scalability of such prototypes from analog deployments to actual space missions (*45*). Challenges specific to legged robots mainly concern the power concept and thermal management. Preliminary results show that these aspects are feasible (*45*, *46*). However, there are currently no powerful space-graded processors to run the mapping, navigation, and locomotion algorithms in real time. In addition, our localization and mapping pipelines heavily rely on LiDARs, which are currently not space-qualified. However, solid-state LiDARs could pave the way for LiDAR-based localization and mapping in space applications. Although there remains substantial room for future research and several open challenges in scaling the presented system to actual space missions, this work is an important step toward teams of legged robots for planetary exploration that provide value in both scientific and commercial missions.

MATERIALS AND METHODS

Hardware description

All described robots here are based on ANYmal by ANYbotics. The Scout is an ANYmal C (2019), whereas the Hybrid and the Scientist are based on ANYmal D (2021). In addition, the Scientist carries a DynaArm, a custom 6-DoF robotic arm. ANYmal weighs 50 kg and has a payload capacity of 15 kg and a nominal operation time of 90 min while continuously walking. We show an overview of the onboard computers in table S4.

Robotic payloads

In the factory configuration, the ANYmals are equipped with a VLP16 Puck LITE LiDAR by Velodyne for mapping and localization, four (ANYmal C) or six (ANYmal D) RealSense D435 active stereo sensors by Intel (front, left, right, and rear) for elevation mapping ("Elevation mapping" section), and two FLIR Blackfly wide-angle cameras (front and rear) to provide RGB image streams. We customized all robots with two high-power, air-cooled LEDs at the front and rear to illuminate dark environments. Because the Scout is the desired mapping robot, we exchanged the four RealSense D435 with two Robosense RS-Bpearl LiDARs (front and rear) for more accurate elevation mapping ("Elevation mapping" section) and dense point cloud mapping ("Dense point cloud mapping" section). In addition, we added Sevensense's Alphasense Core visual-inertial sensor as a high-performance navigation camera array on the Scout. It features three monochrome and four color cameras (front, left, right, and top). Each camera has 0.4 MP and a field of view of 126° by 92.4° (horizontal by vertical). In addition, four high-power, air-cooled LEDs are encapsulated in the same housing. The Alphasense Core allows the operator to quickly gain a first overview in an unknown environment and enables RGB-colored mapping ("Dense point cloud mapping" section).

Science payloads

The Scout carries an ANYbotics inspection payload comprising a 10× optical zoom camera and a spotlight on a pan-tilt unit. We augmented the zoom camera with a spectral filter wheel. The filter wheel contains five narrow band-pass filters (390, 470, 530, 620, and 940 nm) and one position with no filter. In this configuration, we refer to the payload as CTX-FW. We selected CTX-FW to obtain high-resolution images of the targets and their surroundings as well as multispectral information because lunar minerals are known to exhibit distinct reflective features at different wavelengths. On the back of the robot, we mounted a color calibration target with 24 color squares to color-calibrate CTX images.

The Hybrid carries a newer ANYbotics inspection payload for the ANYmal D. It consists of a 20× optical zoom camera, a thermal camera, and a spotlight on a pan-tilt unit. We refer to this payload as CTX-TH. Aside from high-resolution images, CTX-TH enables the thermophysical analysis of targets. Rocks and regolith have different thermal signatures depending on their composition. In addition, we equipped the Hybrid with MIRA, a ruggedized, portable Raman spectrometer (*47*). MIRA is equipped with an auto-focus attachment that enables measurements of targets from a distance of up to 2 m. The MIRA allows compositional analysis of the target's mineralogy, which provides a more in-depth investigation than the CTX-FW and CTX-TH imaging techniques.

The Scientist uses the DynaArm to deploy the instruments for in situ measurements. The DynaArm has a total weight of 10 kg, including the 2.3 kg of the scientific payloads. It has a reach of 0.9 m without any tools attached and a nominal payload capacity of 8 kg at half of the reach with a maximum tool speed of up to 13.5 m/s. The forearm of the DynaArm carries a MIRA. In addition, we mounted our custom-built UV–visible–near IR (UV-VIS-NIR) MICRO as the end effector (fig. S1B). It contains a USB microscope (Dinolite AD4113T-I2V) mounted on a linear actuator mechanism, a ring of 48 RGB LEDs, a time-of-flight (ToF) sensor, and control electronics. The front of the casing is equipped with a foam ring, which ensures that no stray light enters the case when MICRO is in contact with a target. The internal UV and NIR LEDs of the Dino-Lite microscope and the RGB LED ring allow for acquisition of multispectral microscopic images in the entire spectral range from UV to NIR at 395, 470, 525, 620, and 940 nm. The ToF sensor determines the distance between the microscope and the target. The distance feedback allows the microscope, in

combination with the linear actuator and an autofocus routine, to acquire sharp images of the samples, independent of the precise placement of the instrument. Using MICRO′s multispectral images, trained geologists can perform petrographic assessments that are more detailed than the analyses based on CTX-FW.

Legged locomotion in planetary environments

We used a reinforcement learning (RL) approach to design our locomotion policy because RL approaches have shown robust performance in challenging environments (*24*, *25*, *48*). We based our work on the perceptive locomotion pipeline originally published in (*25*), which has already been successfully used in other field deployments such as the DARPA Subterranean Challenge (*49*). In this pipeline, the control policy was trained in two stages: First, we trained a teacher policy with all ground truth information. Then, we trained a student policy to output the same action as the teacher from noisy and limited information.

We used the existing controller from (*25*) on the Scout. On the Hybrid and the Scientist, however, the scientific payloads and the robotic arm can lead to big disturbances for the controller, resulting in reduced robustness and inefficient motion. Therefore, we developed an updated locomotion policy with explicit payload measurements: We added payload mass randomization during the training and explicitly gave the mass information to the teacher policy. Second, we added arm position and velocity observations to allow the policy to actively counteract the wrench on the base caused by the arm′s motion. In addition, we increased the joint torque reward to further improve energy efficiency. During training, we gave a random arm initial position and random arm target position and controlled each arm joint via proportional-derivative (PD) control to simulate the arm movements. We present more detail on our locomotion setup in Supplementary Methods.

Localization, mapping, and perception

In this section, we describe our localization and mapping system, designed to globally localize the robots and generate an accurate representation of the environment during the mission. Furthermore, we describe the instance segmentation algorithm that helps the operations team understand the environment.

Robust LiDAR-based localization

We relied on LiDAR-based simultaneous localization and mapping (SLAM) because of the long range and large field of view of LiDARs. A core challenge of LiDAR-based SLAM in planetary analog missions is LiDAR degeneracy. To cope with degenerate environments, we used a modified version of CompSLAM (*50*), which has been shown to perform well under degeneracy through numerous deployments (*35*). CompSLAM is a complementary multimodal SLAM system based on the Iterative Closest Point algorithm (*51*). CompSLAM can use visual, thermal, or inertial data as a robust prior of the LiDAR mapping module. In this work, we relied only on the inertial data as a prior. If the environment degenerates, CompSLAM identifies degenerate directions and directly uses the prior to integrate the point cloud scan into the map.

Dense point cloud mapping

CompSLAM maintains only a sparse map to keep the SLAM optimization problem tractable. We therefore required a separate module for dense mapping to create a high-resolution environment representation. To this end, we maintained an octree-based map with a voxel size of 30 mm on the robots.

First, we merged and filtered the point clouds of all LiDAR sensors on the robot. After registering the point cloud into the dense map using the pose estimate of the SLAM system, we clipped the map at a 2-m height to remove unnecessary data. Furthermore, we applied an outlier filter by removing points that did not have at least five neighbors within a 200-mm radius. Last, we applied a multirobot crop filter to reject points that lie on the other robots. The mapping pipeline additionally maintained a colorized map by projecting the RGB information from the navigation cameras onto a copy of the point cloud.

After the mission, we fetched the high-resolution point cloud map from the robot, simulating long-term data transmission. First, a GPU-based preprocessor calculated the surface normals at each point using the nearest 40 points. Subsequently, we used a statistical noise filter and a radius filter to filter the map. The statistical noise filter considered the nearest 10 points and filtered out-of-distribution points (SD > 2σ). After the preprocessing, we reconstructed a triangle mesh with a tree depth of 12 using the Poisson surface reconstruction method (*52*) included in the open3D library (*53*) to generate the high-resolution, continuous mesh representation. This process took up to 5 min on a computer with an Intel i9 12700K CPU depending on the terrain complexity. Later, the generated high-resolution mesh was visualized with an eye dome lighting shader (*54*).

Lightweight mesh representation

Because an unreliable, high-latency network cannot transport the dense map in real time, we periodically sent a downsampled version of the dense map (voxel size of 150 mm) in a 9-m radius around the robot to mission control. Before transmission, we compressed the point cloud using the Draco point cloud compression library (*55*). The mission control PC used this downsampled and compressed point cloud to create a lightweight mesh representation (fig. S6). With downsampling and compression, we reduced the size of the point cloud that was transported over the high-latency network from 3 MB to 250 kB. Furthermore, the robot only sent the point cloud if it contained substantial new information, for example, when the robot moved or when the user requested a mesh of a certain area in the user interface. The meshing operation on the mission control PC was limited to a maximum of 0.25 Hz.

The mission control PC calculated a triangle mesh using the Poisson surface reconstruction method (*52*) with a depth parameter of eight. We recalculated the surface normals of the mesh to correct the orientation and smoothness of the mesh surfaces. In addition, we filtered out vertices and triangles with fewer than 10 support points. This mesh was then merged into the mesh map by fusing the nonoverlapped vertices and triangles and averaging the overlapping areas.

Elevation mapping

The elevation map was a local robot-centric 2.5D grid representation where each cell indicated the terrain height. We used it as a terrain representation with a high update rate for the local planning module ("Autonomous local navigation" section). The elevation map is 8 m by 8 m with a resolution of 40 mm. We used an elevation mapping pipeline running on a GPU (*56*) to integrate the point

cloud data into the elevation map in parallel based on the robot's odometry.

Instance segmentation

We applied a boulder instance segmentation network to autonomously identify each boulder instance in the RGB images to contextualize the scientific data. We built our approach on Mask R-CNN (*57*). The network predicts each boulder instance's bounding box, outline, and confidence. We fine-tuned the original model on a custom-built dataset containing hundreds of images collected in the first field trial of the SRC with instance labels. In this custom-built dataset, ANYmal acquired the images in a dark analog lunar terrain, similar to the setting in the final challenge. We deployed our rock instance segmentation network on the mission control PC to segment navigation and CTX images. Figure S7 shows several prediction results, indicating the network's robust performance under variable light conditions and different input cameras.

Scientific payload integration and deployment

The operator could send 3D remote measurement targets to request images from CTX-FW or CTX-TH. For CTX-FW, the operator could additionally specify which spectral filters to use. The operator marked a target on the map or used an already marked target to send a remote measurement task. When requesting RGB images, the operator could select between a high and a low zoom level, with an image width of 0.3 m and 3 m in the focal plane, respectively. The robot sent the images to mission control, which automatically saved them by the target identifier. In addition, the operator could request panoramic images. The robot then took nine images at a fixed zoom level, which were stitched in postprocessing.

The MIRA communicated to the onboard PC of the robot through a USB interface. It was fully integrated into the software stack through a custom Robot Operating System (ROS) wrapper that provided an ROS action interface to trigger a measurement. The measurement procedure was then fully automated: The autofocus attachment measured the distance to the target and focused on this distance, and then the MIRA initiated a measurement. The MIRA matched the received spectroscopic response against the custom-built library of 355 different spectra of relevant lunar minerals (for example, oxides, olivines, pyroxenes, and feldspars) (table S5). The robot sent the spectroscopic response and the corresponding match to mission control for the operations team to evaluate.

The MICRO had a USB interface and communicated to the onboard PC of the robot through rosserial. As for the MIRA, its measurement sequence was fully automated. On a measurement request, the device focused on the target automatically, recorded an image sequence at all available spectral bands (UV, red, green, blue, and NIR), and returned a complete measurement data package.

Payload deployment with the robotic arm

To deploy the MIRA, the arm aligned the Raman laser with the target at the desired distance of 0.7 m. The deployment of MICRO happened in two stages: First, the arm aligned the MICRO with the target pose at a predefined offset of 100 mm in the inverse heading direction of the target pose. In the second stage, a proportional-integral-derivative (PID) controller moved MICRO along the heading axis of the target pose to bring the front foam piece (fig. S1) in contact with the target surface using the ToF distance measurement as feedback. The two-stage approach allowed MICRO to accurately make contact with the target surface, even if the original 6D in situ measurement target was not precisely on the surface. We provide information on the arm controller in Supplementary Methods.

Autonomy

We used behavior trees (BTs) (*58*) to handle the autonomous task execution on the robots. The modularity of BTs allowed us to reuse modules across the different robots. The BT on the robot processed all operator interactions and started, monitored, and stopped the requested task. In this way, the operator set high-level objectives while retaining the ability to stop or change the task easily. We show more details of our BTs in Supplementary Methods.

Autonomous local navigation

The operators guided the robots via high-level navigation goals. We specifically avoided a fully autonomous approach because we preferred that the operations team select and prioritize scientific targets during the mission in unknown environments.

To allow the operator to safely operate the robots via waypoints, we used a sampling-based local planner (*59*) that operated on the local elevation map. Unlike most state-of-the-art navigation planners, it did not assign traversability values to discrete terrain patches. Instead, the robot morphology was approximated by reachability volumes for the feet and a collision volume for the torso, which made the planner more suitable for legged robots. Using a PID controller, a path-tracking module converted the traversable path to twist commands for the locomotion controller.

Autonomous in situ measurement acquisition

Once the Scientist was close to a target, the operator could select the in situ measurement point on the grayscale IR image stream of the Realsense camera. We used the grayscale IR image from the Realsense camera because it did not provide an RGB image stream, and the IR image provided good output in bad lighting conditions. The user interface spawned a 6-DoF interactive marker, which could be adjusted if necessary. The operator could specify the exact measurement task, that is, a MIRA measurement, a MICRO measurement, or both.

Once the robot received the measurement task, it approached the target and aligned the base at a predefined offset of 1 m to the target. Then, the robot deployed the instruments and triggered a measurement automatically. Depending on the task definition, the robot took a MIRA measurement, a MICRO measurement, or both. If an error occurred during the measurement process, the arm moved back to the default position, and the robot notified the operator.

LoS operation

If an LoS occurred, the robots finished their currently allocated task and then switched to a dedicated LoS behavior. The Scout and the Hybrid performed an autonomous measurement routine. First, they recorded a panoramic image of their environment. Second, they imaged their own footprints, which provided information about soil mechanics. Third, the robots acquired images of each other and the Scientist to assess the status of the hardware. Fourth, the Scout took an image of the color calibration card. This image was used in postprocessing to perform color correction.

The robots sent the acquired data to mission control once communication was restored. The Scientist remained in a nominal standing configuration because the system currently does not autonomously detect new measurement targets.

Resilient communication for high-latency networks

Resilient communication in high-latency networks is crucial to ensure data transmission between mission control and the robots. We used commercial off-the-shelf radio devices by Rajant (*60*) to create a reliable mesh network. The mesh setup included the base station and the robots, each acting as a mesh node. The robots were equipped with a BreadCrumb DX2, and the base station consisted of a BreadCrumb ES1 with a panel antenna. All radios operated at 5.8 GHz. The base station and the mission control PCs were connected by wire via a delay simulator that ensured a 5.0-s RTT delay.

We used ROS1 (*61*) on all robots and mission control stations to manage onboard communications. Each robot and mission control station had a separate rosmaster. However, ROS1 was not designed to communicate over high-latency networks, because a TCP handshake is required to establish a connection, even if the data are transmitted over UDP. Therefore, we used Nimbro Network to establish communication between different rosmasters (*62*, *63*). Nimbro Network was specifically designed to work in unreliable high-latency networks and was used in the SpaceBot Cup, a robot competition for lunar exploration (*64*).

Using the predominant internet protocol TCP is problematic because of the RTT delay and high bandwidth. Consequently, we transmitted all data via UDP. UDP does not provide congestion control, and there is no guarantee that data will arrive. Therefore, mission control and the robots only exchanged essential data. We show the network usage of mission control 1 at the SRC in fig. S8. The robot-to-robot communication, however, ran on TCP because the delay was in the low millisecond range.

Supplementary Materials

This PDF file includes:

Results
Methods
Tables S1 to S6
Figs. S1 to S13
References (*65*–*83*)

Other Supplementary Material for this manuscript includes the following:

Movies S1 and S2

REFERENCES AND NOTES

1. L. Qiao, J. W. Head, L. Wilson, Z. Ling, Ina lunar irregular mare patch mission concepts: Distinguishing between ancient and modern volcanism models. *Planet. Sci. J.* **2**, 66 (2021).
2. T. D. Glotch, E. R. Jawin, B. T. Greenhagen, J. T. Cahill, D. J. Lawrence, R. N. Watkins, D. P. Moriarty, N. Kumari, S. Li, P. G. Lucey, M. A. Siegler, J. Feng, L. Breitenfeld, C. C. Allen, H. Nekvasil, D. A. Paige, The scientific value of a sustained exploration program at the Aristarchus Plateau. *Planet. Sci. J.* **2**, 136 (2021).
3. M. Smith, D. Craig, N. Herrmann, E. Mahoney, J. Krezel, N. McIntyre, K. Goodliff, The Artemis program: An overview of NASA's activities to return humans to the moon, in *2020 IEEE Aerospace Conference* (IEEE, 2020), pp. 1–10.
4. A. Colaprete, "Volatiles Investigating Polar Exploration Rover (VIPER)" (NASA Technical Reports, 2021).
5. A. Colaprete, P. Schultz, J. Heldmann, D. Wooden, M. Shirley, K. Ennico, B. Hermalyn, W. Marshall, A. Ricco, R. C. Elphic, D. Goldstein, D. Summy, G. D. Bart, E. Asphaug, D. Korycansky, D. Landis, L. Sollitt, Detection of water in the LCROSS ejecta plume. *Science* **330**, 463–468 (2010).
6. I. G. Mitrofanov, A. B. Sanin, W. V. Boynton, G. Chin, J. B. Garvin, D. Golovin, L. G. Evans, K. Harshman, A. S. Kozyrev, M. L. Litvak, A. Malakhov, E. Mazarico, T. McClanahan, G. Milikh, M. Mokrousov, G. Nandikotkur, G. A. Neumann, I. Nuzhdin, R. Sagdeev, V. Shevchenko, V. Shvetsov, D. E. Smith, R. Starr, V. I. Tretyakov, J. Trombka, D. Usikov, A. Varenikov, A. Vostrukhin, M. T. Zuber, Hydrogen mapping of the lunar south pole using the LRO neutron detector experiment LEND. *Science* **330**, 483–486 (2010).
7. S. Li, P. G. Lucey, R. E. Milliken, P. O. Hayne, E. Fisher, J.-P. Williams, D. M. Hurley, R. C. Elphic, Direct evidence of surface exposed water ice in the lunar polar regions. *Proc. Natl. Acad. Sci. U.S.A.* **115**, 8907–8912 (2018).
8. Z. C. Scoville, Artemis III EVA mission capability for de Gerlache-Shackleton ridge, in *Lunar and Planetary Science Conference* (Lunar and Planetary Institute, 2022).
9. J. Flahaut, J. Carpenter, J.-P. Williams, M. Anand, I. Crawford, W. van Westrenen, E. Füri, L. Xiao, S. Zhao, Regions of interest (ROI) for future exploration missions to the lunar south pole. *Planet. Space Sci.* **180**, 104750 (2020).
10. P. D. Spudis, B. Bussey, J. Plescia, J.-L. Josset, S. Beauvivre, Geology of shackleton crater and the south pole of the moon. *Geophys. Res. Lett.* **35**, L14201 (2008).
11. W. D. Carrier III, G. R. Olhoeft, W. Mendell, Physical properties of the lunar surface, *Lunar Sourcebook, A User's Guide to the Moon* (Cambridge Univ. Press, 1991), pp. 475–594.
12. N. C. Costes, J. E. Farmer, E. B. George, *Mobility Performance of the Lunar Roving Vehicle: Terrestrial Studies, Apollo 15 Results* (NASA, 1972), vol. 401.
13. C. Florenskii, A. Basilevskii, N. Bobina, G. Burba, N. Grebennik, R. Kuzmin, B. Polosukhin, V. Popovich, A. Pronin, L. Ronca, The floor of crater Le Monier—A study of Lunokhod 2 data, in *Lunar and Planetary Science Conference Proceedings* (Lunar and Planetary Institute, 1978), pp. 1449–1458.
14. L. Ding, R. Zhou, Y. Yuan, H. Yang, J. Li, T. Yu, C. Liu, J. Wang, S. Li, H. Gao, Z. Deng, N. Li, Z. Wang, Z. Gong, G. Liu, J. Xie, S. Wang, Z. Rong, D. Deng, X. Wang, S. Han, W. Wan, L. Richter, L. Huang, S. Gou, Z. Liu, H. Yu, Y. Jia, B. Chen, Z. Dang, K. Zhang, L. Li, X. He, S. Liu, K. Di, A 2-year locomotive exploration and scientific investigation of the lunar farside by the Yutu-2 rover. *Sci. Robot.* **7**, eabj6660 (2022).
15. M. Jones, What really happened on Mars Rover Pathfinder, *The RISKS Digest* (1997), pp. 1–2.
16. R. A. Lindemann, D. B. Bickler, B. D. Harrington, G. M. Ortiz, C. J. Voothees, Mars exploration rover mobility development. *IEEE Robot. Autom. Mag.* **13**, 19–26 (2006).
17. J. P. Grotzinger, J. Crisp, A. R. Vasavada, R. C. Anderson, C. J. Baker, R. Barry, D. F. Blake, P. Conrad, K. S. Edgett, B. Ferdowski, R. Gellert, J. B. Gilbert, M. Golombek, J. Gómez-Elvira, D. M. Hassler, L. Jandura, M. Litvak, P. Mahaffy, J. Maki, M. Meyer, M. C. Malin, I. Mitrofanov, J. J. Simmonds, D. Vaniman, R. V. Welch, R. C. Wiens, Mars science laboratory mission and science investigation. *Space Sci. Rev.* **170**, 5–56 (2012).
18. K. A. Farley, K. H. Williford, K. M. Stack, R. Bhartia, A. Chen, M. de la Torre, K. Hand, Y. Goreva, C. D. K. Herd, R. Hueso, Y. Liu, J. N. Maki, G. Martinez, R. C. Moeller, A. Nelessen, C. E. Newman, D. Nunes, A. Ponce, N. Spanovich, P. A. Willis, L. W. Beegle, J. F. Bell III, A. J. Brown, S.-E. Hamran, R. C. Wiens, Mars 2020 mission overview. *Space Sci. Rev.* **216**, 142 (2020).
19. G. Webster, V. McGregor, NASA's Mars Rover has uncertain future as sixth anniversary nears (2009); https://mars.nasa.gov/mer/newsroom/pressreleases/20091231a.html [accessed 27 January 2023].
20. L. David, Opportunity Mars Rover stuck in sand (2005); https://space.com/1019-opportunity-mars-rover-stuck-sand.html [accessed 27 January 2023].
21. N. Potts, A. Gullikson, N. Curran, J. Dhaliwal, M. Leader, R. Rege, K. Klaus, D. Kring, Robotic traverse and sample return strategies for a lunar farside mission to the Schrödinger basin. *Adv. Space Res.* **55**, 1241–1254 (2015).
22. E. S. Steenstra, D. J. Martin, F. E. McDonald, S. Paisarnsombat, C. Venturino, S. O'Hara, A. Calzada-Diaz, S. Bottoms, M. K. Leader, K. K. Klaus, W. van Westrenen, D. H. Needham, D. A. Kring, Analyses of robotic traverses and sample sites in the schrödinger basin for the heracles human-assisted sample return mission concept. *Adv. Space Res.* **58**, 1050–1065 (2016).
23. A. Seeni, B. Schäfer, G. Hirzinger, Robot mobility systems for planetary surface exploration: State-of-the-art and future outlook: A literature survey, in *Aerospace Technologies Advancements* (InTech, 2010), chap. 10, pp. 189–208.
24. J. Lee, J. Hwangbo, L. Wellhausen, V. Koltun, M. Hutter, Learning quadrupedal locomotion over challenging terrain. *Sci. Robot.* **5**, eabc5986 (2020).
25. T. Miki, J. Lee, J. Hwangbo, L. Wellhausen, V. Koltun, M. Hutter, Learning robust perceptive locomotion for quadrupedal robots in the wild. *Sci. Robot.* **7**, eabk2822 (2022).
26. A. Roennau, G. Heppner, M. Nowicki, R. Dillmann, LAURON V: A versatile six-legged walking robot with advanced maneuverability, in *2014 IEEE/ASME International Conference on Advanced Intelligent Mechatronics* (IEEE, 2014), pp. 82–87.
27. S. Dirk, K. Frank, The bio-inspired scorpion robot: Design, control & lessons learned, in *Climbing and Walking Robots: Towards New Applications* (InTech, 2007).

28. S. Bartsch, T. Birnschein, M. Römmermann, J. Hilljegerdes, D. Kühn, F. Kirchner, Development of the six-legged walking and climbing robot SpaceClimber. *J. Field Robot.* **29**, 506–532 (2012).
29. A. Roennau, G. Heppner, M. Nowicki, J. M. Zöllner, R. Dillmann, Reactive posture behaviors for stable legged locomotion over steep inclines and large obstacles, in *2014 IEEE/RSJ International Conference on Intelligent Robots and Systems*, (IEEE, 2014), pp. 4888–4894.
30. H. Kolvenbach, P. Arm, E. Hampp, A. Dietsche, V. Bickel, B. Sun, C. Meyer, M. Hutter, Traversing steep and granular martian analog slopes with a dynamic quadrupedal robot. *Field Robot.* **2**, 910–939 (2022).
31. H. Kolvenbach, D. Bellicoso, F. Jenelten, L. Wellhausen, M. Hutter, Efficient gait selection for quadrupedal robots on the moon and Mars, in *International Symposium on Artificial Intelligence, Robotics and Automation in Space* (I-SAIRAS) (ESA, 2018).
32. H. Kolvenbach, E. Hampp, P. Barton, R. Zenkl, M. Hutter, Towards jumping locomotion for quadruped robots on the moon, in *IEEE/RSJ International Conference on Intelligent Robots and Systems (IROS)* (IEEE, 2019), pp. 5459–5466.
33. N. Rudin, H. Kolvenbach, V. Tsounis, M. Hutter, Cat-like jumping and landing of legged robots in low-gravity using deep reinforcement learning, in *Transactions on Robotics* (IEEE, 2022), vol. 38, pp. 317–328.
34. P. Arm, G. Waibel, G. Ligeza, V. Bickel, M. Tranzatto, S. Zimmermann, T. Homberger, L. Horvath, H. Umbers, F. Kehl, H. Kolvenbach, M. Hutter, Results and lessons learned from the first field trial of the ESA-ESRIC space resources challenge of team GLIMPSE, in *16th Symposium on Advanced Space Technologies in Robotics and Automation (ASTRA 2022)* (ESA, 2022).
35. M. Tranzatto, T. Miki, M. Dharmadhikari, L. Bernreiter, M. Kulkarni, F. Mascarich, O. Andersson, S. Khattak, M. Hutter, R. Siegwart, K. Alexis, Cerberus in the DARPA subterranean challenge. *Sci. Robot.* **7**, eabp9742 (2022).
36. N. Hudson, F. Talbot, M. Cox, J. Williams, T. Hines, A. Pitt, B. Wood, D. Frousheger, K. L. Surdo, T. Molnar, R. Steindl, M. Wildie, I. Sa, N. Kottege, K. Stepanas, E. Hernandez, G. Catt, W. Docherty, B. Tidd, B. Tam, S. Murrell, M. Bessell, L. Hanson, L. Tychsen-Smith, H. Suzuki, L. Overs, F. Kendoul, G. Wagner, D. Palmer, P. Milani, M. O'Brien, S. Jiang, S. Chen, R. C. Arkin, Heterogeneous ground and air platforms, homogeneous sensing: Team CSIRO Data61's approach to the DARPA subterranean challenge. arXiv:2104.09053 [cs.RO] (19 April 2021).
37. A. Agha, K. Otsu, B. Morrell, D. D. Fan, R. Thakker, A. Santamaria-Navarro, S.-K. Kim, A. Bouman, X. Lei, J. Edlund, M. F. Ginting, K. Ebadi, M. Anderson, T. Pailevanian, E. Terry, M. Wolf, A. Tagliabue, T. S. Vaquero, M. Palieri, S. Tepsuporn, Y. Chang, A. Kalantari, F. Chavez, B. Lopez, N. Funabiki, G. Miles, T. Touma, A. Buscicchio, J. Tordesillas, N. Alatur, J. Nash, W. Walsh, S. Jung, H. Lee, C. Kanellakis, J. Mayo, S. Harper, M. Kaufmann, A. Dixit, G. Correa, C. Lee, J. Gao, G. Merewether, J. Maldonado-Contreras, G. Salhotra, Maira Saboia Da Silva, B. Ramtoula, Y. Kubo, S. Fakoorian, A. Hatteland, T. Kim, T. Bartlett, A. Stephens, L. Kim, C. Bergh, E. Heiden, T. Lew, A. Cauligi, T. Heywood, A. Kramer, H. A. Leopold, C. Choi, S. Daftry, O. Toupet, I. Wee, A. Thakur, M. Feras, G. Beltrame, G. Nikolakopoulos, D. Shim, L. Carlone, J. Burdick, Nebula: Quest for robotic autonomy in challenging environments; TEAM CoSTAR at the DARPA subterranean challenge. arXiv:2103.11470 [cs.RO] (21 March 2021).
38. M. J. Schuster, M. Müller, S. G. Brunner, H. Lehner, P. Lehner, R. Sakagami, A. Dömel, L. Meyer, B. Vodermayer, R. Giubilato, M. Vayugundla, J. Reill, F. Steidle, I. von Bargen, K. Bussmann, R. Belder, P. Lutz, W. Stürzl, M. Smísek, M. Maier, S. Stoneman, A. Prince, B. Rebele, M. Durner, E. Staudinger, S. Zhang, R. Pöhlmann, E. Bischoff, C. Braun, S. Schröder, E. Dietz, S. Frohmann, A. Börner, H. Hübers, B. Foing, R. Triebel, A. Albu-Schäffer, A. Wedler, The arches space-analogue demonstration mission: Towards heterogeneous teams of autonomous robots for collaborative scientific sampling in planetary exploration. *IEEE Robot. Autom. Lett.* **5**, 5315–5322 (2020).
39. F. Cordes, I. Ahrns, S. Bartsch, T. Birnschein, A. Dettmann, S. Estable, S. Haase, J. Hilljegerdes, D. Koebel, S. Planthaber, Lunares: Lunar crater exploration with heterogeneous multi robot systems. *Intell. Serv. Robot.* **4**, 61–89 (2011).
40. R. Sonsalla, F. Cordes, L. Christensen, T. M. Roehr, T. Stark, S. Planthaber, M. Maurus, M. Mallwitz, E. A. Kirchner, Field testing of a cooperative multi-robot sample return mission in Mars analogue environment, in *14th Symposium on Advanced Space Technologies in Robotics and Automation (ASTRA)* (ESA, 2017).
41. Boston Dynamics, Search for life: NASA JPL explores martian-like caves (2022); https://youtube.com/watch?v=qTW-dbZr4U8 [accessed 23 January 2023].
42. T. Tzanetos, M. Aung, J. Balaram, H. F. Grip, J. T. Karras, T. K. Canham, G. Kubiak, J. Anderson, G. Merewether, M. Starch, M. Pauken, S. Cappucci, M. Chase, M. Golombek, O. Toupet, M. C. Smart, E. B. Ramirez, N. Chahat, R. Hogg, B. Pipenberg, M. Keennon, K. H. Williford, Ingenuity Mars helicopter: From technology demonstration to extraterrestrial scout, in *2022 IEEE Aerospace Conference (AERO)* (IEEE, 2022) pp. 1–19.
43. M. Hutter, C. Gehring, A. Lauber, F. Gunther, C. D. Bellicoso, V. Tsounis, P. Fankhauser, R. Diethelm, S. Bachmann, M. Bloesch, H. Kolvenbach, M. Bjelonic, L. Isler, K. Meyer, ANYmal —Toward legged robots for harsh environments. *Adv. Robot.* **31**, 918–931 (2017).
44. H. A. Oravec, V. M. Asnani, C. M. Creage, S. J. Moreland, Geotechnical review of existing mars soil simulants for surface mobility. *Earth Space* **2021**, 157–170 (2021).
45. H. Kolvenbach, M. Breitenstein, C. Gehring, M. Hutter, Scalability analysis of legged robots for space exploration, in *68th International Astronautical Congress (IAC 2017)* (Curran, 2018), pp. 10399–10413.
46. G. Valsecchi, D. Liconti, F. Tischhauser, H. Kolvenbach, M. Hutter, Preliminary design of actuators for walking robot on the moon, in *16th Symposium on Advanced Space Technologies in Robotics and Automation (ASTRA 2022)* (ESA, 2022).
47. Metrohm, Metrohm MIRA XTR DS (2023); https://metrohm.com/en/products/raman-spectroscopy/mira-ds-mira-xtr-ds.html [accessed 23 January 2023].
48. X. B. Peng, E. Coumans, T. Zhang, T.-W. Lee, J. Tan, S. Levine, Learning agile robotic locomotion skills by imitating animals. arXiv:2004.00784 [cs.RO] (2 April 2020).
49. M. Tranzatto, M. Dharmadhikari, L. Bernreiter, M. Camurri, S. Khattak, F. Mascarich, P. Pfreundschuh, D. Wisth, S. Zimmermann, M. Kulkarni, V. Reijgwart, B. Casseau, T. Homberger, P. De Petris, L. Ott, W. Tubby, G. Waibel, H. Nguyen, C. Cadena, R. Buchanan, L. Wellhausen, N. Khedekar, O. Andersson, L. Zhang, T. Miki, T. Dang, M. Mattamala, M. Montenegro, K. Meyer, X. Wu, A. Briod, M. Mueller, M. Fallon, R. Siegwart, M. Hutter, K. Alexis, Team CERBERUS wins the DARPA subterranean challenge: Technical overview and lessons learned. arXiv:2207.04914 [cs.RO] (11 July 2022).
50. S. Khattak, H. Nguyen, F. Mascarich, T. Dang, K. Alexis, Complementary multi–modal sensor fusion for resilient robot pose estimation in subterranean environments, in *2020 International Conference on Unmanned Aircraft Systems (ICUAS)* (IEEE, 2020), pp. 1024–1029.
51. K.-L. Low, Linear least-squares optimization for point-to-plane ICP surface registration (University of North Carolina, 2004), pp. 1–3.
52. M. Kazhdan, M. Bolitho, H. Hoppe, Poisson surface reconstruction, in *Eurographics Symposium on Geometry Processing*, K. Polthier, A. Sheffer, Eds. (Eurographics, 2006), vol. 7.
53. Q.-Y. Zhou, J. Park, V. Koltun, Open3D: A modern library for 3D data processing. arXiv:1801.09847 [cs.CV] (30 January 2018).
54. C. Boucheny, "Interactive scientific visualization of large datasets: Towards a perceptive-based approach," thesis, Université Joseph Fourier Grenoble, France (2009).
55. Google, Draco 3D graphics compression (2017); https://google.github.io/draco/ [accessed 27 January 2023].
56. T. Miki, L. Wellhausen, R. Grandia, F. Jenelten, T. Homberger, M. Hutter, Elevation mapping for locomotion and navigation using GPU, in *2022 IEEE/RSJ International Conference on Intelligent Robots and Systems (IROS)* (IEEE, 2022), pp. 2273–2280.
57. K. He, G. Gkioxari, P. Dollár, R. Girshick, Mask r-cnn, in *Proceedings of the IEEE International Conference on Computer Vision* (IEEE, 2017), pp. 2961–2969.
58. D. Faconti, "Mood2be: Models and tools to design robotic behaviors" (Technical Report, Eurecat Centre Tecnologic, 2019), vol. 4.
59. L. Wellhausen, M. Hutter, Rough terrain navigation for legged robots using reachability planning and template learning, in *2021 IEEE/RSJ International Conference on Intelligent Robots and Systems (IROS)* (IEEE, 2021), pp. 6914–6921.
60. Rajant, https://rajant.com/products/breadcrumb-wireless-nodes/dx-series/ [accessed 9 January 2023].
61. M. Quigley, K. Conley, B. Gerkey, J. Faust, T. Foote, J. Leibs, R. Wheeler, A. Y. Ng, Ros: An open-source robot operating system, in *ICRA Workshop on Open Source Software* (IEEE, 2009), p. 5.
62. J. Stückler, M. Schwarz, M. Schadler, A. Topalidou-Kyniazopoulou, S. Behnke, Nimbro explorer: Semiautonomous exploration and mobile manipulation in rough terrain. *J. Field Robot.* **33**, 411–430 (2016).
63. M. Schwarz, T. Rodehutskors, D. Droeschel, M. Beul, M. Schreiber, N. Araslanov, I. Ivanov, C. Lenz, J. Razlaw, S. Schüller, D. Schwarz, A. Toplaidou-Kyniazopoulou, S. Behnke, Nimbro rescue: Solving disaster-response tasks with the mobile manipulation robot Momaro. *J. Field Robot.* **34**, 400–425 (2017).
64. T. Kaupisch, D. Noelke, A. Arghir, DLR SpaceBot Cup 2013: A space robotics competition, in *Symposium on Advanced Space Technologies in Robotics and Automation (ASTRA)* (ESA, 2015).
65. S. Lee, S. Jeon, J. Hwangbo, Learning legged mobile manipulation using reinforcement learning, in *Robot Intelligence Technology and Applications 7: Results from the 10th International Conference on Robot Intelligence Technology and Applications* (Springer, 2023), pp. 310–317.
66. Z. Fu, X. Cheng, D. Pathak, Deep whole-body control: Learning a unified policy for manipulation and locomotion, in *Conference on Robot Learning (CoRL)* (OpenReview, 2022).
67. Y. Ma, F. Farshidian, T. Miki, J. Lee, M. Hutter, Combining learning-based locomotion policy with model-based manipulation for legged mobile manipulators. *IEEE Robot. Autom. Lett.* **7**, 2377–2384 (2022).
68. F. Farshidian, R. Grandia, M. Spieler, J. Carius, J.-P. Sleiman, Ocs2 (2022); https://leggedrobotics.github.io/ocs2/ [accessed 27 September 2022].

69. J.-R. Chiu, J.-P. Sleiman, M. Mittal, F. Farshidian, M. Hutter, A collision-free mpc for whole-body dynamic locomotion and manipulation, in *2022 International Conference on Robotics and Automation (ICRA)* (IEEE, 2022), pp. 4686–4693.
70. J. Sleiman, F. Farshidian, M. V. Minniti, M. Hutter, A unified MPC framework for whole-body dynamic locomotion and manipulation. *IEEE Robot. Autom. Lett.* **6**, 4688–4695 (2021).
71. J. L. Blanco-Claraco, A tutorial on SE(3) transformation parameterizations and on-manifold optimization. arXiv:2103.15980 [cs.RO] (29 March 2021).
72. F. Abi-Farraj, N. Pedemonte, P. Robuffo Giordano, A visual-based shared control architecture for remote telemanipulation, in *2016 IEEE/RSJ International Conference on Intelligent Robots and Systems (IROS)* (IEEE, 2016), pp. 4266–4273.
73. D. Faconti, Behaviortree.cpp (2022); https://behaviortree.dev/ [accessed 5 October 2022].
74. JPL, A description of the rover Sojourner; https://mars.nasa.gov/MPF/rover/descrip.html [accessed 27 January 2023].
75. NASA, Mars exploration rovers overview; https://mars.nasa.gov/mer/mission/rover/wheels-and-legs/ [accessed 27 January 2023].
76. L. Ding, R. Zhou, T. Yu, H. Gao, H. Yang, J. Li, Y. Yuan, C. Liu, J. Wang, Y. Zhao, Surface characteristics of the Zhurong Mars rover traverse at Utopia Planitia. *Nat. Geosci.* **15**, 171–176 (2022).
77. M. Heverly, J. Matthews, M. Frost, C. Quin, Development of the tri-athlete lunar vehicle prototype, in *Proceedings of the 40th Aerospace Mechanisms Symposium* (NASA, 2010).
78. DFKI, CREX: Crater Explorer; https://robotik.dfki-bremen.de/en/research/robot-systems/crex/ [accessed 27 January 2023].
79. P. Arm, R. Zenkl, P. Barton, L. Beglinger, A. Dietsche, L. Ferrazzini, E. Hampp, J. Hinder, C. Huber, D. Schaufelberger, F. Schmitt, B. Sun, B. Stolz, H. Kolvenbach, M. Hutter, SpaceBok: A dynamic legged robot for space exploration, in *IEEE International Conference on Robotics and Automation (ICRA)* (IEEE, 2019).
80. R. Playter, M. Buehler, M. Raibert, BigDog, in *Unmanned Systems Technology VIII* (SPIE, 2006), pp. 896–901.
81. Boston Dynamics, Spot specifications; https://support.bostondynamics.com/s/article/Robot-specifications [accessed 27 January 2023.
82. ANYbotics, ANYmal specifications; https://anybotics.com/anymal-autonomous-legged-robot/ [accessed 27 January 2023].
83. B. Katz, J. Di Carlo, S. Kim, Mini cheetah: A platform for pushing the limits of dynamic quadruped control, in *2019 International Conference on Robotics and Automation (ICRA)* (IEEE, 2019), pp. 6295–6301.

Acknowledgments: We would like to thank the implementation partners, namely, the Lucerne University of Applied Sciences and Arts (HSLU), ANYbotics AG, and the maxon SpaceLab. A special thanks to S. Tenisch, A. Brandes, G. Székely, and N. Steinert for developing the filter wheel; F. Mast, L. Horvath, H. Umbers, and M. Trentini for supporting the MICRO development; and D. Larcher and J. Bernasconi for supporting the scientific data analysis. We would like to thank Metrohm Schweiz AG for providing the Raman spectrometer. We acknowledge the ETH Earth Sciences Collections and the University of Basel for supporting and providing rock and mineral samples for our experiments. We thank KIBAG Kies Neuheim AG for making the quarry available. This work has been conducted as part of ANYmal Research, a community to advance legged robotics. **Funding:** This research was supported by the Swiss National Science Foundation (SNF) through the National Centre of Competence in Research Robotics (NCCR Robotics), through the National Centre of Competence in Digital Fabrication (NCCR dfab), and by ETH Zurich Research grant no. 21-1 ETH-27. This project has received funding from the European Research Council (ERC) under the European Union's Horizon 2020 research and innovation programme grant agreement nos. 852044 and 101016970. This project has received funding through ESA contract nos. 4000137333/22/NL/AT and 4000135310/21/NL/PA/pt. **Author contributions:** All authors contributed to the system design and wrote the paper. P.A., G.W., J.P., T.T., R.Z., V.B., G.L., F.K., and H.K. participated in the field deployments and evaluated the respective data. P.A., G.W., J.P., and T.M. conducted the additional locomotion tests. T.T. and R.Z. developed the mapping and perception pipelines. J.P. developed the arm controller. T.M. developed the locomotion controller. V.B., G.L., and F.K. selected and designed the scientific payloads and evaluated the respective data. **Competing interests:** The authors declare that they have no competing interests. **Data and materials availability:** All data needed to evaluate the conclusions in the paper are present in the paper or the Supplementary Materials. Other materials are available at Zenodo (DOI: 10.5281/zenodo.8019960).

Submitted 14 October 2022
Accepted 12 June 2023
Published 12 July 2023
10.1126/scirobotics.ade9548

Science Robotics

Scientific exploration of challenging planetary analog environments with a team of legged robots

Philip Arm, Gabriel Waibel, Jan Preisig, Turcan Tuna, Ruyi Zhou, Valentin Bickel, Gabriela Ligeza, Takahiro Miki, Florian Kehl, Hendrik Kolvenbach, and Marco Hutter

Sci. Robot. **8** (80), eade9548. DOI: 10.1126/scirobotics.ade9548

Science Robotics (ISSN 2470-9476) is published by the American Association for the Advancement of Science. 1200 New York Avenue NW, Washington, DC 20005. The title *Science Robotics* is a registered trademark of AAAS.